PHYSICAL REVIEW C **85**, 054004 (2012)

Cross-section measurements of ^{2}H(n, np)n in symmetric star configurations

A. H. Couture,[1,*] T. B. Clegg,[2,†] S. Tajima,[2,3,4] C. R. Howell,[2,3] B. Fallin,[2,3] J. H. Esterline,[2,3] A. S. Crowell,[2,3] B. J. Crowe,[2,4] D. M. Markoff,[2,4] L. C. Cumberbatch,[2,4] R. S. Pedroni,[2,5] and H. Witała[6]

[1]*Department of Physics and Astronomy, University of North Carolina at Chapel Hill, Chapel Hill, North Carolina 27599, USA*
[2]*Triangle Universities Nuclear Laboratory (TUNL), Durham, North Carolina 27708, USA*
[3]*Department of Physics, Duke University, Durham, North Carolina 27708, USA*
[4]*Department of Physics, North Carolina Central University, Durham, North Carolina 27707, USA*
[5]*Department of Physics, North Carolina A, and T State University, Greensboro, North Carolina 27411, USA*
[6]*Institute of Physics, Jagiellonian University, PL-30059 Cracow, Poland*

(Received 3 March 2012; published 16 May 2012)

Cross-section measurements have been made at 16 and 19 MeV in two exit-channel configurations of neutron-deuteron breakup: the space star and coplanar star. In this kinematically complete measurement, the outgoing proton and one of the neutrons were detected in coincidence and their energies were determined via time-of-flight techniques. Monte Carlo simulations based on rigorous three-nucleon Faddeev calculations using the charge-dependent-Bonn (CD-Bonn) nucleon-nucleon potential were used to compare the experimental results with theory. Large discrepancies between data and theory were found in both breakup configurations measured at both energies, suggesting deficiencies in current theoretical treatment of three-nucleon forces or in present knowledge of the neutron-neutron $^1S_0$ force.

DOI: 10.1103/PhysRevC.85.054004 PACS number(s): 13.75.Cs, 21.45.Ff, 25.10.+s, 25.40.−h

I. INTRODUCTION

An extensive compilation of proton-proton (pp) and neutron-proton (np) scattering data has been cataloged over the last half century [1]. Nuclear force models have been tailored to describe these data, and constants of these models enable fits to np or pp scattering phase shifts with a χ^2 per degree of freedom close to one [2–4]. Comparison of np and pp phase shifts provides information about charge dependence of the nucleon-nucleon (NN) interaction for different orbital angular momentum and spin combinations. However, the situation is not as clear with regards to charge symmetry because of the lack of pure neutron-neutron (nn) scattering data.

The three-nucleon ($3N$) system provides a theoretically solid platform for examining how features of NN potential models are manifested in a system where charge-dependent and multinucleon forces are important. The neutron-deuteron (nd) system is ideal because the Coulomb interaction is not present, thereby reducing the complexity of the theoretical treatment of the system. When NN models are used to describe pairwise interactions in $3N$ calculations, the results agree well with low-energy experimental data in most cases. However, there are some notable exceptions: the triton binding energy defect [5,6], the nucleon-deuteron analyzing power (A_y) puzzle [7], and the space-star (SST) anomaly [8]. Attempts have been made to resolve these problems by including a $3N$ force ($3N$F). The binding energy of the triton may be reproduced using $3N$ forces; however, the A_y puzzle and the space-star anomaly remain unresolved.

In the SST configuration of nd breakup, three nucleons exit the reaction in the c.m. system in a plane perpendicular to the incident neutron beam with momenta of equal magnitude and pairwise angular separation of 120 degrees. The space-star anomaly is a discrepancy between theoretical predictions and experimental measurements of the five-fold differential breakup cross section, $d^5\sigma/d\Omega_1 d\Omega_2 dS$, for the SST. The data are systematically higher than theory at all energies where measurements have been made. This anomaly has been established by eight previous measurements taken at incident neutron beam energies of 10.3, 13.0, 16.0, and 25.0 MeV. Three of these experiments were performed in Germany at Bochum [9] and Erlangen [10,11], one at the Chinese Institute of Atomic Energy [12], and four at TUNL [13–15].

Considering the successful agreement between theoretical predictions and measurement for other observables [16], one may question the validity of the experimental cross sections for the SST configuration, especially given the experimental challenges of measuring absolute cross sections using nn coincidence techniques. All previous measurements were taken with essentially the same experimental setup, the common features being (1) the two outgoing neutrons were detected in coincidence, (2) the scatterer was a deuterated scintillator allowing measurement of the energy of the outgoing proton, and (3) the target-beam integrated luminosity was determined through ^{2}H(n, n)^{2}H elastic scattering. In this technique a substantial fraction of the systematic errors result from uncertainties in the absolute efficiencies of the two neutron detectors and in estimating the effects of neutron scattering in the target scintillator. Because of the possibility of systematic errors that are either underestimated or unaccounted for that are common to all previous experiments, we have made new measurements using a technique that has different sources of systematic errors than previous experiments. Our experiment uses a technique similar to that developed by Huhn *et al.* [17,18] for measuring the nn scattering length. The primary distinctions between our technique and those used in previous SST measurements

---

[*] acouture@tunl.duke.edu
[†] http://www.tunl.duke.edu

are (1) the outgoing proton was detected in coincidence with one of the neutrons, (2) the deuterated target was a thin CD_2 foil to allow outgoing protons to exit the target and have their momentum measured, and (3) the integrated target-beam luminosity was determined by $^2H(n,d)n$ elastic scattering. Our technique does not have thick target effects and only depends on knowledge of the efficiency of one neutron detector. In addition to taking SST cross-section data, measurements were made for the coplanar star (CST) configuration of the *nd* breakup reaction in which the plane defined by the momenta of the outgoing nucleons also contains the incident beam.

II. EXPERIMENTAL DETAILS

A. Neutron beam

The neutron beam used in this experiment was produced via the $^2H(d,n)^3He$ reaction in the Shielded Source Area of TUNL. This reaction has a +3.3 MeV Q-value, which provides a more than 5 MeV separation from the dominant background neutron source reactions, $^2H(d,n)dp$ and $^2H(d,n)ppn$. The neutron production gas cell was a copper tube with a 0.5-mm-thick gold beam stop soldered to one end and a 6.35-μm-thick Havar beam-entrance foil on the other end. The gas chamber within the cell was 71.4 mm long and filled to 7.8 atm with 99.99% pure research grade deuterium gas. Distilled water was pumped through copper cooling coils surrounding the gas cell in a closed water circulation loop to remove the heat generated by stopping the beam in the cell. The temperature of the water in the closed loop was maintained by heat exchange with a laboratory 50 °C chilled-water system. Air cooling was also directed at the gold beam stop and the Havar foil. The entire gas cell was electrically isolated from the remainder of the beam pipe and the current deposited on the beam stop was sent to a beam-current integrator (BCI).

The target area was shielded from the neutron production cell and other upstream sources of neutron and gamma radiation by a wall composed of concrete, steel, lead, and paraffin. The concrete and paraffin were included for low-energy neutron shielding, while the steel and lead were used to deflect higher-energy neutrons and γ rays [19]. The neutron beam was shaped by a 115-cm-long, double-truncated copper collimator with a circular cross section that connected the neutron production cell to the target area. This collimator produced a roughly uniform, 40-mm-diameter neutron beam at the location of the CD_2 target, 187 cm from the neutron production cell.

The main source of target correlated background in the *nd* breakup measurements was due to events from the same reaction induced by the lower-energy neutrons in the incident beam. To estimate and subtract this background from the events caused by the 16 and 19 MeV neutrons required knowledge of the energy distribution of the incident neutron beam, which was determined using time-of-flight (ToF) techniques. The energy spectrum of the neutron beam was measured using an organic liquid scintillator with a cylindrical volume (5.08 cm diameter, 5.08 cm depth) placed in the neutron beam at a center-to-center distance of 376 cm from the neutron production cell. The deuteron beam was "chopped and bunched" [20] at a rate of 78.1 kHz into packets with a width of ~3 ns. The pulsed beam allowed ToF measurement of the neutron energies using the delayed signal from a capacitive pickoff unit located just before the gas cell. The γ peak in the ToF spectrum provided a time reference. The width of the prompt neutron peaks determined by the ToF measurements is not representative of the actual beam energy distribution, but is instead determined by the width of the pulsed deuteron beam packets. A better estimation of the width of this peak was obtained by calculating the deuteron beam energy loss as it passed through the deuterium gas column in the gas cell. This method provided a width of 0.34 (0.28) MeV for the prompt 16.0 (19.0) MeV neutron peak. Graphs comparing the raw neutron energy distribution measured via ToF with the deconvoluted energy spectrum that resulted from removing the effects due to the time spread in of the deuteron beam pulses are shown in Fig. 1 for 16 and 19 MeV. The energy spread in the highest-energy neutron group in the beam was due to the energy loss of the deuterons in the gas cell.

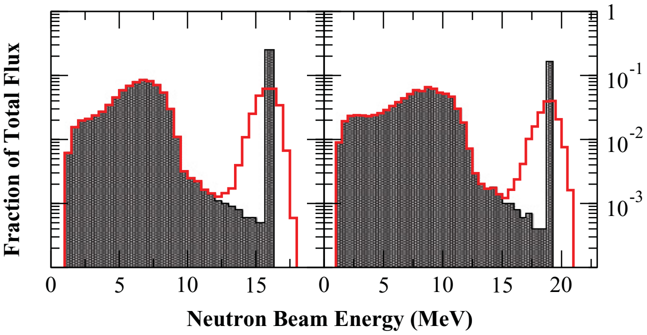

FIG. 1. (Color online) Neutron beam energy distribution measured by ToF using a pulsed neutron beam. The measured distribution is shown as the solid (red) line. The shaded (black) region shows the deconvoluted distribution (the energy smearing arising from the time spread of the deuteron beam pulses was removed) that was used in the data analysis. The graph on the left (right) shows the 16.0 (19.0) MeV results.

B. Target chamber

The experimental setup is shown in Fig. 2. The main components of the setup are the target chamber and the particle detectors. The target chamber is described in this section, and the description of the charged-particle and neutron detectors will follow. An interior view of the target chamber is shown in Fig. 3. The target rod has two 76.2-mm-square aluminum frames for mounting targets. For this experiment a deuterated polyethylene (CD_2) foil was mounted in one frame, and the other frame was empty to allow background measurements without disturbing the vacuum system. The CD_2 foils had a circular cross section and were 25.4 mm in diameter. The CD_2 foil was suspended at the center of the aluminum frame by thin nylon strings. The CD_2 foil used in the 16.0 MeV measurements was 22.4 mg/cm^2 thick and that used in the 19.0 MeV measurements was 29.8 mg/cm^2.

FIG. 2. (Color online) Three-dimensional renderings of top, front, and perspective views of experimental setup showing the target chamber (T), the charged particle arms (P), the SST (S) and CST (C) neutron detectors, and the neutron beam (red arrow). Please note that, in the front view, the neutron beam direction is out of the page.

The center part of the target chamber (i.e., the scattering chamber) is made from a from a 0.635-cm-thick cylindrical stainless steel cylinder 17.1 cm high and 34.3 cm in diameter. The spherical lid for the cylinder was made from 0.318 cm thick aluminum to allow the neutrons emitted from the CD_2 target to exit the chamber with uniform and negligible scattering effects. The vacuum in the chamber was maintained at 10^{-5} Torr by a turbo-molecular pump. The neutron beam entered the chamber through a 7.6-cm-diameter, 100-μm-thick beryllium window. The beam, as well as neutrons emitted by the target, exited the chamber through a 25-μm-thick rectangular tantalum window (6.4 cm × 2.0 cm). This window was wide enough to pass neutrons from the CST configuration within the solid angle of the neutron detectors for that configuration.

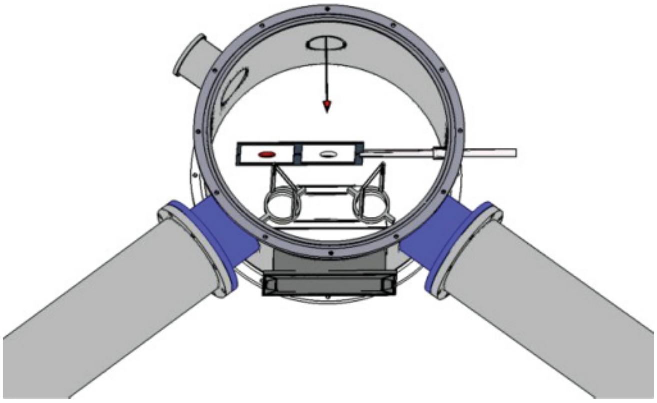

FIG. 3. (Color online) Illustration of target chamber. The neutron beam axis is shown by the red arrow. The target rod holds the CD_2 foil. The two ΔE detectors are held in the frames between the target and the proton arms.

Two arms containing E-ΔE detector pairs were attached to the scattering chamber on opposite sides of the incident neutron beam axis and in the horizontal plane. The E-ΔE detector combination was used to identify and measure the momentum of protons and deuterons emitted from the target at the angles given in Table I. The energy of the charged particles was determined with better than 20% resolution via ToF measurements between the ΔE and E detectors. However, the overall energy spread in the detected charged particles was larger than the measurement resolution and was dominated by the energy loss in the CD_2 foil. The ΔE detectors were mounted through ports in the bottom plate of the scattering chamber that positioned the ΔE detectors as close as possible to the target without being in the path of the neutrons emitted at the angles of the SST and CST configurations being measured. More details about the charged-particle detector arms are given in the next section.

C. Particle detectors

Surveyed detector angles and distances for the experimental setup are given in Table I. The charged particle arms of the scattering chamber each housed an E-ΔE telescope. Each ΔE detector consisted of a 4.7-mg/cm^2-thick BC-404 plastic scintillator coupled to a Hamamatsu 1949-51 photomultiplier tube (PMT). The plastic scintillator was covered with a thin (about 5 μm) aluminum tent to reflect scintillator light into the PMT. The center of the plastic scintillator in the ΔE detectors was located 8 cm from the CD_2 target. The minimum energy required for a proton to traverse the ΔE detector and its aluminum tent was 1.7 MeV, while a deuteron needed 2.2 MeV for transmission. The E detector in each arm consisted of a 10-cm-diameter by 5-mm-thick disk of BC-404 plastic scintillator coupled to a Hamamatsu H6527 PMT. The front face of the scintillator was located 61 cm from the ΔE detector and was covered with thin aluminum foil to serve as a light reflector and seal. The foil did not affect the ToF energy measurements with the exception of stopping the slowest charged particles.

All neutron detectors used in this experiment were of the same design. They were manufactured by the Bicron Corporation and were filled with BC-501A liquid organic scintillating fluid. The fluid chamber consisted of an aluminum cylinder (12.68 cm diameter, 5.08 cm long) capped by a 1-mm-thick aluminum plate on one end and a glass window on the other. A Teflon tube connected to the liquid chamber was coiled around the cell to allow for thermal expansion of the fluid. The cell and tube are designed such that no gas bubbles were present in the active scintillating volume. The interior aluminum surfaces of the fluid chamber were painted with BC-622 reflective polyurethane resin so that scintillated light exited only through the glass window. This window was directly coupled to a 12.7-cm-diameter model R1250 Hamamatsu PMT encased in a mu-metal shield.

TABLE I. Detector central angles, distances, and properties. The polar angle θ is given with respect to the direction of the incident neutron beam. The azimuthal angle ϕ is measured from the beam right in the horizontal scattering plane. Detector distances are given from target center to the surface of the scintillator for the charged particle (E) detectors and to the center of the scintillator volume for the neutron (N) detectors.

Detector	θ (deg)	ϕ (deg)	Distance (cm)	Diameter (cm)	Thickness (cm)	Scint. type
E1	51.3 ± 0.5	180.0 ± 0.1	69.0 ± 0.2	10.0 ± 0.05	0.50 ± 0.02	BC-404
E2	52.3 ± 0.5	0.0 ± 0.1	69.0 ± 0.2	10.0 ± 0.05	0.50 ± 0.02	BC-404
N1	51.4 ± 0.5	119.5 ± 0.5	73.0 ± 0.2	12.68 ± 0.05	5.08 ± 0.05	BC-501A
N2	51.7 ± 0.5	59.7 ± 0.5	73.1 ± 0.2	12.68 ± 0.05	5.08 ± 0.05	BC-501A
N3	17.7 ± 0.5	180.0 ± 0.5	101.3 ± 0.2	12.68 ± 0.05	5.08 ± 0.05	BC-501A
N4	18.7 ± 0.5	0.0 ± 0.5	102.4 ± 0.2	12.68 ± 0.05	5.08 ± 0.05	BC-501A

III. THEORETICAL CALCULATIONS AND MONTE CARLO SIMULATIONS

The theoretical cross-section predictions for *nd* breakup and elastic scattering were made using rigorous Faddeev calculations and different modern NN potentials alone or combined with 3NF models [16,21]. Predictions were made using either the CD-Bonn [2], the Argonne v_{18} (AV18) [3], or the Nijmegen I or II [4] NN potentials. Each of these four NN-potential models were also combined with the Tucson-Melbourne (TM99) 3NF [22,23] using cutoff Λ values which led to a reproduction of the ^{3}H binding energy for a particular NN force and TM99 combination. The AV18 NN potential was also combined with the Urbana (UIX) 3NF [24]. In addition to the above (semi)phenomenological NN interactions, ten different NN chiral potentials were used, five at next-to-next-to-leading order (N^{2}LO) and five at next-to-next-to-next-to-leading order (N^{3}LO) of chiral expansion [25]. These potentials differ in the value of the high-momentum cutoffs used in their construction. Using a particular pair of cutoffs, Λ and $\tilde{\Lambda}$, their low-energy constants were then adjusted to reproduce two-nucleon phase shifts. All choices of these cutoff values described the two-nucleon system equally well. The first nonvanishing 3NF appears in N^{2}LO order of the chiral expansion [26]. Each of the five N^{2}LO potentials were combined with a chiral N^{2}LO 3NF using matching high-momentum cutoffs. The two adjustable strength parameters appearing in the short-range terms of that 3NF were adjusted for each NN chiral potential to reproduce the triton binding energy and the *nd* scattering length [26]. The Faddeev calculations for all of these different potential models predict *nd* breakup cross sections which differ by less than ±1% for the SST configurations.

These calculations are for point geometry; that is, they assume a monoenergetic neutron beam with a target and detectors of infinitesimal size. To make a meaningful comparison of experimental data with the theoretical predictions, Monte Carlo (MC) simulations were performed to average the point geometry calculations over the finite geometry of our experiment. Along with this averaging process several other effects were included in the simulation: the energy loss and attenuation of charged particles in the target and ΔE detectors, background events from low-energy neutrons in the beam, and the time resolution of the detectors and electronics.

The *nd* elastic scattering cross-section library contained differential cross sections for the ^{2}H$(n,n)^2$H reaction in the c.m. frame calculated using the CD-Bonn [2] potential model for incident neutron energies from 0.5 to 20 MeV in 0.5 MeV steps. At each energy, the library contained cross-section values for neutron scattering angles in the c.m. system in 2.5° steps from 0° to 180°.

The *nd* breakup library was more extensive as a result of the additional degrees of freedom in three-body kinematics. This library contained files consisting of five-fold differential cross sections, $d^5\sigma/d\Omega_n d\Omega_p dS$, in the laboratory frame, also based on the CD-Bonn [2] potential specified by four variables: the incident neutron energy E_n^0 and the outgoing nucleon angles θ_p, θ_n, and ϕ_{np}. These four parameters define the S curve, the locus of all kinematically allowed pairs of detected nucleon energies on the E_p vs E_n plane. Each file contains differential cross sections generated in 0.1 MeV steps along the S curve. The incident neutron beam energies used to produce the libraries were based on the energy distribution of the incident neutron beams shown in Fig. 1 beginning at 5.0 MeV and increasing in 0.5 MeV steps. The library entries for the highest energy neutron group at 16.0 and 19.0 MeV were made in finer steps with points at the maximum-, central-, and minimum-energy values of the peak. The cross-section libraries were composed to span 1° to 2° beyond the physical angular acceptance of the detectors to ensure complete coverage. The angular ranges and step sizes for the CST and SST configurations incorporated in the libraries are summarized in Table II. In all more than 60 000 files for different combinations of E_n^0, θ_p, θ_n, and ϕ_{np}, each containing on average about 175 points along the S curve, were included in the breakup cross-section library.

IV. DATA ANALYSIS

Data analysis was divided into three parts: (1) determination of the number of valid breakup events from the experimental data for the SST and CST configurations, (2) prediction of

TABLE II. Angular ranges and increments used to generate theoretical cross-section libraries for the *nd* breakup Monte Carlo simulation.

Configuration	θ_n (deg)	θ_p (deg)	ϕ_{np} (deg)
CST range	13.0–24.0	46.0–58.0	159–180
CST increment	1.1	1.0	3.0
SST range	44.5–59.5	46.0–58.0	104–136
SST increment	1.5	1.0	3.0

the number of breakup events that should have been measured using $3N$ theory calculations and MC simulations, and (3) comparison of data to simulations. Comparing the measured counts to the predicted counts should be equivalent to comparing finite-geometry cross-section data to Faddeev calculations averaged over the geometry and energy resolution of the experiment. One advantage of comparing counts instead of cross sections is that statistical and systematic uncertainties can be cleanly separated into experiment and theory, respectively. That is, because the measured counts have only statistical uncertainties, all systematic errors in the method are assigned exclusively to the theoretical predictions.

A. Experimentally measured counts

In our technique for measuring the nd breakup reaction the proton and one of the neutrons were detected in coincidence. A valid breakup event was tagged as one in which the proton was cleanly identified in the ΔE-E arm and the associated neutron detected within a window of 200 ns. Identity of the charged particles was done using the relationship between ToF and kinetic energy. The different particle species in the ΔE-E arm are separated into distinct bands in two-dimensional ToF vs pulse-height spectra as shown in Fig. 4. Gates were set around the proton and deuteron bands as illustrated in Fig. 4. The liquid scintillators used for neutron detection are sensitive to both neutrons and γ rays. Pulse-shape analysis of the decay of the scintillation light is used to distinguish these two species. A sample pulse-shape discrimination (PSD) spectrum is shown in Fig. 5 with a gate around the neutron region.

The nucleon energies involved in neutron-proton coincidences were determined by ToF measurements and plotted on the E_p versus E_n plane. In an idealized experiment, using a neutron beam with a delta-function energy spectrum and point-geometry beam, target, and detectors, all coincident counts would lie on the kinematic locus. However, as a result of the finite geometry of the experimental setup, the measured coincidences are found in a band around the ideal locus. The location and width of the band was determined using the Monte Carlo simulation. A two-dimensional gate was set around this region of the proton-versus-neutron-energy spectrum to obtain the number of breakup events as described below.

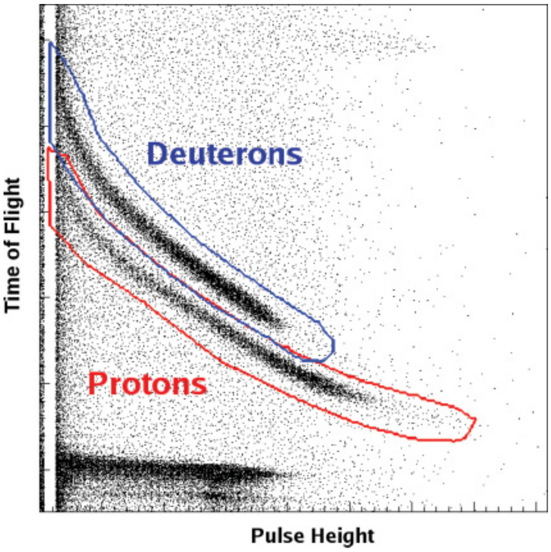

FIG. 4. (Color online) Charged particle identification spectrum. The plot of pulse height vs ToF separates particles with the same energy but different masses into bands. The upper (blue) gate is for deuterons, the lower (red) gate is for protons. Both axes have a linear scale with arbitrary units.

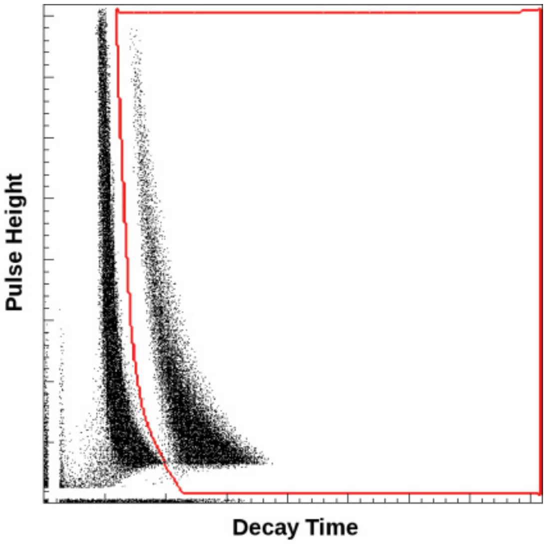

FIG. 5. (Color online) Neutron pulse-shape discrimination spectrum. The graph shows the total energy deposited in the scintillator (pulse height) versus the decay time of the anode signal. The (red) gate was set around the neutrons. Counts outside the gate were caused by γ-rays. The units on both axes are arbitrary.

Along with the true nd breakup coincidence events of interest, background coincidence events were measured as well. Accidental coincidences may have occurred between time-uncorrelated events that were misidentified as breakup events. Such events form a uniform background in both the proton and neutron time spectra. One or both of the signals in a coincident event may be caused by processes uncorrelated with nd breakup. To remove these events from the analysis, unphysical regions of the timing spectra corresponding to particles traveling faster than the speed of light were used to determine the magnitude of the accidental coincidence background. The physical region of the spectra containing nd breakup events will be referred to as the "true + accidental" (T + A) region and the unphysical region will be referred to as the "accidental" (A) region. Gates of identical shape were set on the T + A and A regions. To assign energies to the A region, the ToF for events in that region was shifted such that the A gate identically overlapped with the T + A gate.

There are four possible combinations of proton and neutron event types, as shown in Table III. Two-dimensional (2D) spectra of the N3-E2 CST detector pair for each of these event types are graphed in Fig. 6. The measured locus containing the true nd breakup events along with background coincidences corresponds to event type (a). The same 2D gate was applied to each event type and the coincident events within the gate were projected into 1 MeV bins along the neutron energy axis.

TABLE III. Identification of true and accidental event types. The coincident event type was used to refer to the combination of proton- and neutron-event types.

Coincidence event type	Proton event type	Neutron event type
(a)	T + A	T + A
(b)	A	T + A
(c)	T + A	A
(d)	A	A

The measured locus has coincident events of type (b), (c), and (d) as backgrounds. The accidental spectra for coincident events of type (b) and (c) each have events of type (d) as a background. The projected counts in the T + A gate and the net counts arising from the accidental background are plotted in Fig. 7 for the CST configuration at 16 MeV. To remove the accidental background from the measured locus the following formula was applied:

$$\begin{aligned} Y(T) &= Y(a) - [Y(b) - Y(d)] - [Y(c) - Y(d)] - Y(d) \\ &= Y(a) - Y(b) - Y(c) + Y(d). \end{aligned} \tag{1}$$

Here $Y(T)$ is the estimated yield of true nd breakup events in a particular neutron energy bin and $Y(i)$ is the projected yield of the ith coincident event type into that same bin. The statistical uncertainty for the true yields is given by

$$\Delta Y(T) = \sqrt{Y(a) + Y(b) + Y(c) + Y(d)}. \tag{2}$$

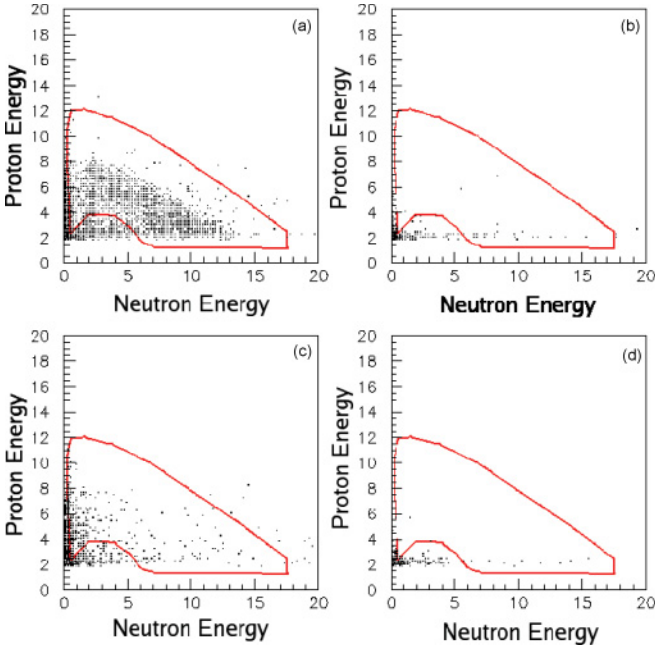

FIG. 6. (Color online) Measured locus and accidental spectra for N3-E2 CST detector pair at 16.0 MeV incident neutron energy. The letter in the top right corner of each spectrum indicates the coincident event type as defined in Table III. The (red) gate defines the region where nd breakup events are kinematically allowed. The units on all axes are MeV.

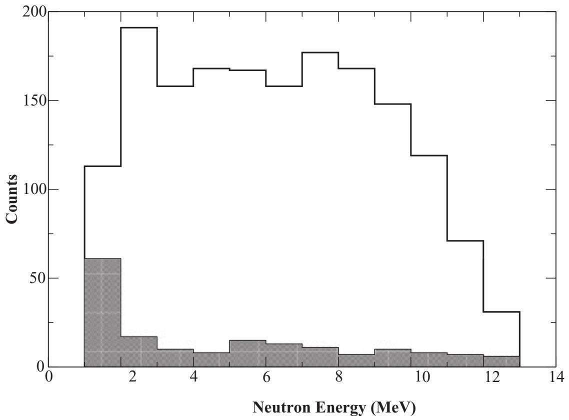

FIG. 7. Measured energy spectra of T + A (unshaded) and net accidental coincidence (shaded) events for the N3-E2 CST coincidence pair at 16.0 MeV incident neutron energy. These spectra are produced by projecting the counts in the gates in E_n-vs-E_p 2D histogram onto the E_n axis.

There is also a source of nonaccidental background which may not be accounted for by the methods described above. The neutron beam used in this experiment contains low-energy neutrons which may induce real nd breakup events that pollute our coincidence spectra. The Monte Carlo simulation was used to determine the fraction of true nd breakup counts in each neutron energy bin which were caused by these low-energy neutrons and corrections were applied to the measured spectra.

B. Theoretically predicted counts

The number of nd breakup events, $Y_{nd\mathrm{bu}}$, in an energy bin along the E_n axis was predicted from the effective cross section $d^5\sigma/d\Omega_n d\Omega_p dE_n$ produced by the Monte Carlo simulation using the following relationship:

$$Y_{nd\mathrm{bu}} = \left(\frac{d^5\sigma}{d\Omega_n d\Omega_p dE_n}\right) tn\Omega_p\Omega_n\varepsilon_n\alpha_n E_n f_{LT}, \tag{3}$$

where t, n, Ω, ε_n, α_n, E_n, and f_{LT} stand for the target thickness, neutron beam flux, detector solid angles, neutron detector efficiency, neutron attenuation, energy bin width, and fractional live time of the data acquisition system, respectively. The proton detector is assumed to be 100% efficient, and the attenuation of the protons in the target, the ΔE detector and the aluminum foil in front of the E detector is handled by the Monte Carlo simulation and accounted for in the effective cross section. The product of the target thickness, neutron beam flux, proton detector solid angle, and live time were determined via nd elastic scattering performed simultaneously with the nd breakup experiment. These quantities are related to the elastic cross section and yield as follows:

$$tn\Omega_p f_{LT} = \frac{Y_{nde}}{\left(\frac{d\sigma}{d\Omega}\right)_{nde}}. \tag{4}$$

Many elastically scattered deuterons were stopped in either the target or ΔE detectors and thus were not recorded. However, the total number of elastic scattering events is the

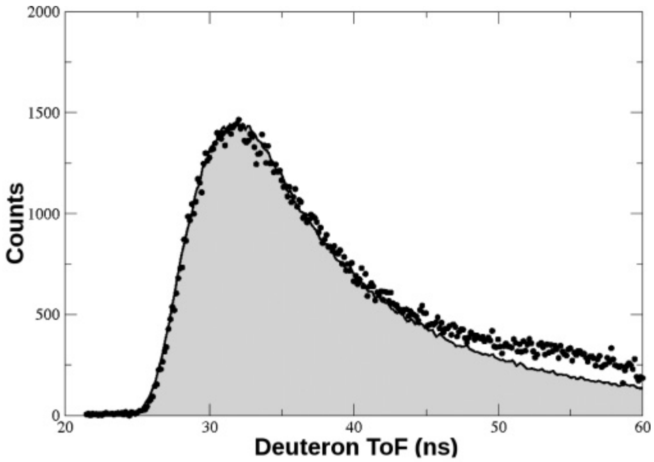

FIG. 8. Comparison of elastic Monte Carlo spectrum to data. The solid black curve is the Monte Carlo simulation for a 16.0 MeV run. The black dots are the measured data.

quantity needed in Eq. (4). This issue, along with the fact that the low-energy region of the elastic deuteron spectrum was contaminated with substantial background, led to the adoption of the following procedure for *nd* elastic scattering normalization.

The high-energy region of the elastic deuteron spectrum was used to determine the total *nd* elastic yield by fitting this part of the spectrum with the Monte Carlo simulation. The full *nd* elastic yield was estimated using the following equation:

$$Y_{nde} = Y_{nde}^{\mathrm{HE}} \left(\frac{Y_{\mathrm{MC}} \left\langle \frac{d\sigma}{d\Omega} \right\rangle_{nde}}{Y_{\mathrm{MC}}^{\mathrm{HE}} \left\langle \frac{d\sigma}{d\Omega} \right\rangle_{nde}^{\mathrm{HE}}} \right), \tag{5}$$

where the superscript HE indicates the high-energy region of the deuteron spectrum. Variables without the HE designation represent the total *nd* elastic process. In the above equation the yields with the HE designation come from summing over the HE region, and the cross section with the HE tag is the average cross section in the high-energy region. The yields with the MC subscript are from the MC simulated spectrum and those with *nde* subscript are from the measured spectrum. Combining Eqs. (3)–(5) we obtain the following expression containing all quantities used to predict the *nd* breakup yields:

$$Y_{nd\mathrm{bu}} = \left(\frac{d^5\sigma}{d\Omega_n d\Omega_p dE_n} \right) \Omega_n \varepsilon_n \alpha_n E_n \times \left(\frac{Y_{nde}^{\mathrm{HE}} Y_{\mathrm{MC}}}{Y_{\mathrm{MC}}^{\mathrm{HE}} \left\langle \frac{d\sigma}{d\Omega} \right\rangle_{nde}^{\mathrm{HE}}} \right). \tag{6}$$

The ToF spectrum created by the Monte Carlo simulation was fit to the measured data taken by each charged particle arm on a batch-by-batch basis. The MC spectrum was binned such that the width of one bin corresponded to the width of one time-to-digital-converter (TDC) channel (0.135 ns). As seen in Fig. 8, the high-energy region of the ToF spectrum shows excellent agreement between data and simulation, while the lower-energy region is less successful. The reason for this discrepancy at low energies is twofold: the deuteron energy-loss calculations in the Monte Carlo simulation become unreliable at very low energies, and the signal-to-noise ratio is quite bad in the low-energy region of the measured spectrum. For these reasons only the high-energy region of the ToF spectrum was used in the fit with the cutoff energy being chosen based on χ^2 minimization.

The sources of systematic error in this experiment are as follows:

(i) *nd* elastic normalization. This includes contributions from uncertainties in background subtraction, calculation of deuteron energy loss, detector angle position, fitting the deuteron energy spectrum, and the *nd* elastic scattering cross section.
(ii) Background subtraction of breakup events from low-energy neutrons. This was governed by the uncertainty in the change in *nd* breakup cross section with energy and the incident neutron beam energy spectrum.
(iii) Neutron detector solid angle. The uncertainty was derived from the measurement error in the neutron flight paths (±2 mm).
(iv) Neutron detector efficiency. The detector efficiencies were determined with measurements at TUNL using the ^{2}H(d,n)^{3}He source reaction as well as the spontaneous fission of a ^{252}Cf source. These measurements were each compared to a simulated spectrum. The uncertainty in the detector efficiencies was derived from two main sources: (i) a ±3% uncertainty stemming from the range of normalizations needed to bring the measured spectra in agreement with the simulation for the various detectors and (ii) a ±1% uncertainty associated with small deviations in the shape of the measured spectra. These uncertainties were added in quadrature to produce an overall systematic error of ±3.2%.
(v) Neutron attenuation. This was only relevant for the SST neutrons since they passed through the aluminum chamber dome. The systematic uncertainty assigned to this quantity was based upon a first-order estimate of isotropic, energy-independent neutron-aluminum scattering.
(vi) Neutron energy binning. The width of the neutron energy bins into which the measured counts were projected was determined by the energy calibration. Uncertainty in the measurement of the nanoseconds per TDC channel used in this experiment provide an estimate of the systematic error in the width of the 1 MeV energy binning.
(vii) Theoretical calculations. The cross-section predictions produced by Faddeev calculations using a variety of potential models had a spread of 1% for the star configurations at both energies.

The estimates for the relative error of each of these contributions were added in quadrature to estimate the systematic error for the entire experiment. Table IV shows the contribution of each of the sources of systematic error.

TABLE IV. Summary of systematic uncertainties inherent in the breakup cross-section measurement.

Source of uncertainty	Estimated uncertainty	
	16 MeV	19 MeV
Elastic normalization	±4.0%	±4.7%
Background subtraction	±2.0%	±2.0%
Solid angle	±0.3%	±0.3%
Detector efficiency	±3.2%	±3.2%
Neutron attenuation (SST)	±1.0%	±1.0%
Energy binning	±1.0%	±1.0%
Theoretical Calculation	±1.0%	±1.0%
Total uncertainty (SST)	±5.7%	±6.3%
Total uncertainty (CST)	±5.7%	±6.2%

C. Data and simulation comparison

The results for the SST and CST cross-section measurements at 16 and 19 MeV are shown in Fig. 9. The data are the statistically weighted averages of the counts measured by the mirrored detector pairs for each breakup configuration in 1 MeV bins along the neutron energy. Background events have been subtracted from these spectra. The error bars on the data reflect only statistical uncertainty. The solid black lines in the figures are the theoretical predictions produced by the Monte Carlo simulation based on the CD-Bonn [2] potential; the blue band around them gives the systematic uncertainty. The results at the two energies are quite similar. The SST data agree with theoretical predictions at the lowest-detected neutron energies. As the energy of the detected neutron increases the data lie well above the theoretical curve, with theory ∼35% below data at the location of the SST. The CST data agree with theoretical predictions quite well at all detected neutron energies except in the region of the star configuration where data are below theory by ∼30% in the 16 MeV results and ∼40% for 19 MeV. The discrepancy between the theoretical cross-section predictions and the actual values should be directly proportional to the relative difference between the measured and predicted counts. All previous measurements of the SST reported the differential cross section with respect to S, $d^5\sigma/d\Omega_1 d\Omega_2 dS$. The current results must be presented in the same manner to compare them with those measurements. To do this, the relative discrepancy between the measured counts and predicted counts found around the star condition was assumed to be equal to that for cross-section comparisons between data and theory with respect to S.

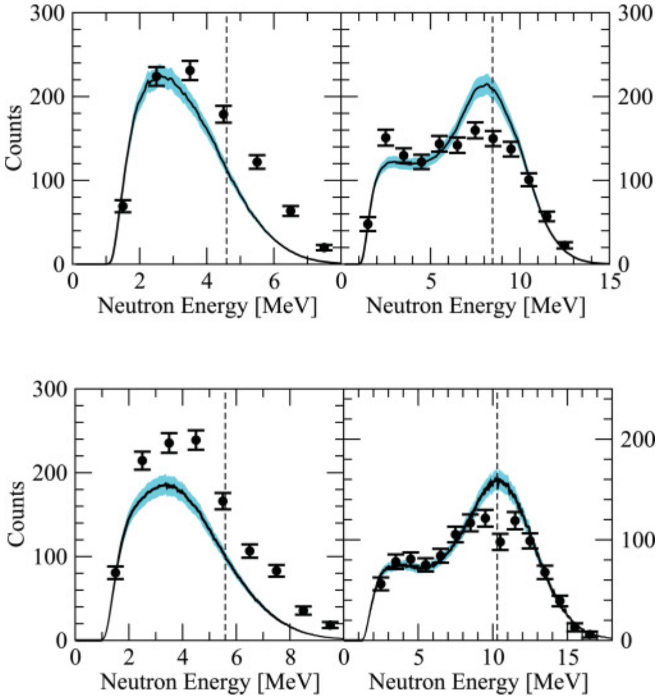

FIG. 9. (Color online) Counts measured (solid dots) for the SST (left) and CST (right) configurations taken at incident neutron beam energies of 16.0 MeV (top) and 19.0 MeV (bottom) compared to theoretical predictions based on the CD-Bonn potential (solid curve), taking into account experimental energy and angular resolution via Monte Carlo simulations. Error bars on the data points are statistical uncertainty. The shaded (blue) band around the theoretical prediction is systematic uncertainty. Table IV provides the magnitude and sources of this uncertainty. The position of the star condition is indicated by the vertical dashed line.

The SST cross section measured in the current experiment is ∼25% larger than the measurement of Crowell [14]. Considering the combined uncertainties of the two experiments, this represents a 2σ discrepancy. Figure 10 shows the values for the current experiment compared with the history of SST cross-section measurements. Table V compares theoretical point-geometry cross sections for both configurations at both energies to estimated cross sections based on the measurements reported in this paper.

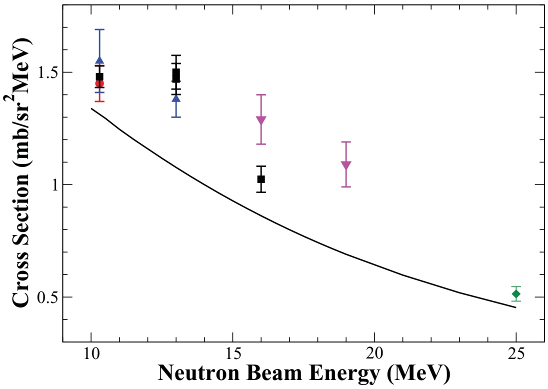

FIG. 10. (Color online) History of SST cross-section measurements with present data included. The data points for the present work shown as the (magenta) inverted triangles were created by calculating the relative discrepancy between the number of counts measured and the number of counts predicted by the CD-Bonn potential. This discrepancy was then used to estimate the point-geometry cross section by simple multiplication. Point-geometry SST cross sections based on the CD-Bonn potential are given by the black curve. Previous SST cross-section data taken at Bochum [9], Erlangen [10,11], TUNL [13–15], and CIAE [12] are shown as (red) circles, (blue) triangles, (black) squares, and (green) diamonds, respectively. The error bars for all data on this graph represent statistical and systematic errors added in quadrature. Please note the suppressed zero on the y axis.

TABLE V. Comparison of point-geometry star cross sections based on the CD-Bonn potential to estimates based upon the data collected in this experiment.

Configuration	Beam energy	Cross section (mb/sr^2 MeV)	
		CD-Bonn	Measured
SST	16 MeV	0.86	1.29 ± 0.11
CST	16 MeV	2.21	1.61 ± 0.14
SST	19 MeV	0.69	1.09 ± 0.10
CST	19 MeV	2.03	1.25 ± 0.13

V. DISCUSSION

The SST cross section has been shown to be insensitive to the choice of NN potential model and to the action of a 3NF [13–15]. To determine the most significant contributing partial waves, cross sections were calculated using only the $^1S_0$, only $^3S_1$-$^3D_1$, the combination of these two, and all higher angular momentum components of the CD-Bonn interaction up to a two-body total angular momentum, $j = 3$. The results of these calculations are shown im Fig. 11. These studies show that the SST cross section is built predominantly from the singlet and triplet S-wave components of the NN force with the triplet being the dominant of the two. The effects of higher partial waves on the star cross sections are essentially negligible. Both the $^1S_0$ and $^3S_1$-$^3D_1$ np forces have been well determined by np scattering data and the properties of the deuteron [1,27]. Up to this point, the $^1S_0$ nn force has been determined only indirectly because of the lack of free nn data [28,29]. Therefore, one might expect that the $^1S_0$ nn force is the most likely culprit for the disagreement between data and theory in the star configurations.

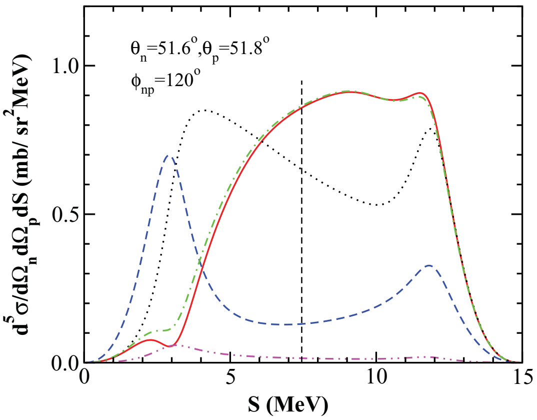

FIG. 11. (Color online) Sensitivity of the SST five-fold point-geometry cross section $d^5\sigma/d\Omega_n d\Omega_p dS$ based on the CD-Bonn potential to different partial waves as a function of S, the arc length along the kinematic locus. The solid (red) line shows the full calculation with all partial waves up to $j_{\max} = 3$ included. The dashed (blue), dotted (black), and dashed-dotted (green) lines show the results when only contributions from $^1S_0$, $^3S_1$-$^3D_1$, and $^1S_0$ + $^3S_1$-$^3D_1$ are kept when calculating the cross sections, respectively. The dashed-double-dotted (magenta) line presents contribution of all partial waves with the exception of $^1S_0$ and $^3S_1$-$^3D_1$. The position of the star condition is indicated by the vertical dashed line.

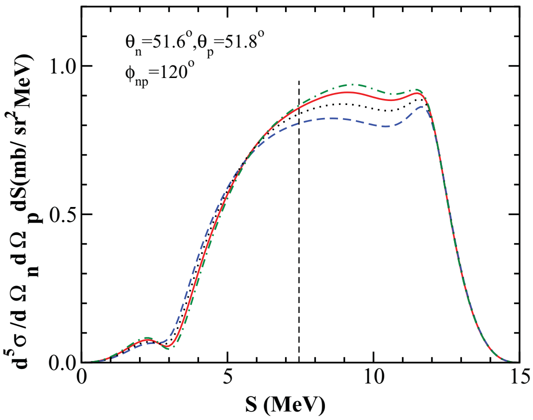

FIG. 12. (Color online) Sensitivity of SST five-fold point-geometry cross section $d^5\sigma/d\Omega_n d\Omega_p dS$ to the changes of the nn $^1S_0$ force component. Those changes were induced by multiplying the $^1S_0$ nn matrix element of the CD-Bonn potential by a factor λ. The solid (red) line is the full result based on the original CD-Bonn potential [2] and all partial waves with 2N total angular momenta up to $j_{\max} = 3$ included. The dashed (blue), dotted (black), and dashed-dotted (green) lines correspond to $\lambda = 0.9$, 0.95, and 1.05, respectively.

Significant discrepancies have also been found in the nn quasi-free-scattering (QFS) breakup geometries [30,31]. The QFS configuration refers to an exit channel of nd breakup in which one of the nucleons is at rest in the laboratory system. In nd breakup, the nn or np QFS configurations are possible, leaving the proton or one of the neutrons at rest, respectively. Measurements of nd breakup cross sections have been performed at $E_n^{\text{lab}} = 26$ MeV for nn and np QFS [30]; as well as at $E_n^{\text{lab}} = 25$ MeV for nn QFS [31]. The results for nn QFS resemble those of the SST, showing measured cross sections ≈20% higher than theoretical predictions. Surprisingly, when instead of the nn pair the np pair is quasifreely scattered, the theory closely follows the np QFS cross-section data [30]. Just as with the SST, theoretical predictions for QFS cross sections have minimal dependence upon the NN potential used in the calculations and do not change significantly with the addition of 3NFs [16,32].

A sensitivity study of low-energy QFS cross sections [32] showed that nn QFS is extremely sensitive to the $^1S_0$ nn force component, in contrast to np QFS which is insensitive to such change. In the study of Ref. [32] a very simple mechanism was used to change the $^1S_0$ nn interaction. The $^1S_0$ nn matrix element of the CD-Bonn potential was multiplied by a factor λ. This technique demonstrated that the nn QFS undergoes significant variations while the np QFS cross sections remain essentially unchanged. The increase in the $^1S_0$ nn force strength ($\lambda = 1.08$) needed to bring the nn QFS theoretical cross sections into agreement with data would lead to a nearly bound state of two neutrons. The corresponding study for the SST configuration, however, shows that changes which would provide an explanation for the nn QFS have almost no effect on the SST discrepancy [32]. In Fig. 12, we present evidence that increasing the strength of the $^1S_0$ nn interaction by 5% has only 1% effect on the SST cross section near the star condition, far less than is needed to account for the discrepancy between experiment and theory.

Despite the extreme stability of SST cross sections to underlying dynamics, the possibility that some exotic and long-ranged components of a 3NF will influence nd breakup cross sections may not be excluded. Chiral perturbation theory in orders higher than N^{2}LO introduces a multitude of additional short- and long-range 3NF contributions which come with a variety of momentum-spin dependencies [33]. These contributions to χEFT 3NF have yet to be put into a form applicable to numerical Faddeev calculations to check their effects on SST cross sections. First steps in this direction have been made in Ref. [34].

Considering the study of the large nn QFS discrepancies, one may also speculate that the existence of a two-neutron bound state could affect star cross sections. Such a state could not only change the predicted SST cross sections by the drastic change of the $^1S_0$ nn interaction, but also influence measured cross sections in an indirect way by providing a continuous background from the reaction $n + {}^2\mathrm{H} \to p + {}^2n \to p + n + n$, which would be particularly important in regions of the breakup phase space with small cross sections, like the SST configuration.

In summary, we have presented cross-section data for the symmetric star configurations of nd breakup at incident neutron beam energies of $E_n^{\mathrm{lab}} = 16$ and 19 MeV. These data have been taken by detecting the outgoing np pair in coincidence, while all previous SST measurements have detected the nn pair. Thus the clear discrepancy between data and theory found in the present measurement supports those revealed in previously reported experiments. Because of the striking insensitivity of the theoretical cross sections to the underlying dynamics, such large discrepancies would require new long-ranged components of 3NFs or could even indicate a deficiency in our present knowledge of the $^1S_0$ nn force.

ACKNOWLEDGMENTS

This work was partially supported financially by US Department of Energy Office of Nuclear Physics Grants No. DE-FG02-97ER41033, No. DE-97ER41041, and No. DE-05ER41380, and by the National Science Foundation CREST Grant No. HRD-0833184. It was also partially supported by the Polish National Science Center as research project no. DEC-2011/01/B/ST2/00578. The numerical calculations were performed on the supercomputer cluster of the JSC, Jülich, Germany.

[1] V. G. J. Stoks, R. A. M. Klomp, M. C. M. Rentmeester, and J. J. de Swart, Phys. Rev. C **48**, 792 (1993).

[2] R. Machleidt, Phys. Rev. C **63**, 024001 (2001).

[3] R. B. Wiringa, V. G. J. Stoks, and R. Schiavilla, Phys. Rev. C **51**, 38 (1995).

[4] V. G. J. Stoks, R. A. M. Klomp, C. Terheggen, and J. J. de Swart, Phys. Rev. C **49**, 2950 (1994).

[5] T. Sasakawa and S. Ishikawa, Few-Body Syst. **1**, 3 (1986).

[6] C. R. Chen, G. L. Payne, J. L. Friar, and B. F. Gibson, Phys. Rev. C **33**, 1740 (1986).

[7] W. Tornow, J. Esterline, and G. Weisel, J. Phys. G: Nucl. Part. Phys. **35**, 125104 (2008).

[8] C. Howell *et al.*, Nucl. Phys. A **631**, 692C (1998).

[9] M. Stephan *et al.*, Phys. Rev. C **39**, 2133 (1989).

[10] J. Strate *et al.*, Nucl. Phys. A **501**, 51 (1989).

[11] K. Gebhardt *et al.*, Nucl. Phys. A **561**, 232 (1993).

[12] Z. Zhou *et al.*, Nucl. Phys. **684**, 545C (2001).

[13] H. Setze *et al.*, Phys. Rev. C **71**, 034006 (2005).

[14] A. Crowell, Ph.D. thesis, Duke University, 2001.

[15] R. Macri, Ph.D. thesis, Duke University, 2004.

[16] W. Glöckle, H. Witała, D. Hüber, H. Kamada, and J. Golak, Phys. Rep. **274**, 107 (1996).

[17] V. Huhn, L. Wätzold, Ch. Weber, A. Siepe, W. von Witsch, H. Witała, and W. Glöckle, Phys. Rev. Lett. **85**, 1190 (2000).

[18] V. Huhn, L. Wätzold, Ch. Weber, A. Siepe, W. von Witsch, H. Witała, and W. Glöckle, Phys. Rev. C **63**, 014003 (2000).

[19] D. Glasgow *et al.*, Nucl. Instrum. Methods **114**, 521 (1974).

[20] C. Howell, Ph.D. thesis, Duke University, 1984.

[21] D. Hüber, H. Kamada, H. Witała, and W. Glöckle, Acta Phys. Pol. B **28**, 1677 (1997).

[22] S. A. Coon and W. Glöckle, Phys. Rev. C **23**, 1790 (1981).

[23] S. A. Coon and H. Han, Few-Body Syst. **30**, 131 (2001).

[24] B. S. Pudliner, V. R. Pandharipande, J. Carlson, S. C. Pieper, and R. B. Wiringa, Phys. Rev. C **56**, 1720 (1997).

[25] E. Epelbaum, Prog. Part. Nucl. Phys. **57**, 654 (2006).

[26] E. Epelbaum, A. Nogga, W. Glöckle, H. Kamada, Ulf-G. Meissner, and H. Witała, Phys. Rev. C **66**, 064001 (2002).

[27] B. Bergervoet, P. C. van Campen, R. A. M. Klomp, J. L. deKok, T. A. Rijken, V. G. J. Stoks, and J. J. deSwart, Phys. Rev. C **41**, 1435 (1990).

[28] E. Konobeevski, Phys. At. Nucl. **73**, 1302 (2010).

[29] A. Gardestig, J. Phys. G: Nucl. Part. Phys. **36**, 053001 (2009).

[30] A. Siepe *et al.*, Phys. Rev. C **65**, 034010 (2002).

[31] X. Ruan *et al.*, Phys. Rev. C **75**, 057001 (2007).

[32] H. Witała and W. Glöckle, J. Phys. G: Nucl. Part. Phys. **37**, 064003 (2010).

[33] V. Bernard, E. Epelbaum, H. Krebs, and U.-G. Meißner, Phys. Rev. C **77**, 064004 (2008).

[34] R. Skibinski *et al.*, Phys. Rev. C **84**, 054005 (2011).